

Mode-coupling approach to near-cuspidal patterns in planar fluid flows

Rodolfo Brandão^{1,*}, Gabriel D. Carvalho^{2,†} and José A. Miranda^{2,‡}

¹*Department of Mathematics, Imperial College London, London SW7 2AZ United Kingdom*

²*Departamento de Física, Universidade Federal de Pernambuco, Recife, Pernambuco 50670-901 Brazil*



(Received 21 March 2021; accepted 24 May 2021; published 7 June 2021)

We investigate the evolution of the interface separating two Newtonian fluids of different viscosities in two-dimensional Stokes flow driven by suction or injection. A second-order, mode-coupling theory is used to explore key morphological aspects of the emerging interfacial patterns in the stage of the flow that bridges the purely linear and fully nonlinear regimes. In the linear regime, our analysis reveals that an injection-driven expanding interface is stable, while a contracting motion driven by suction is unstable. Moreover, we find that the linear growth rate associated with this suction-driven instability is independent of the viscosity contrast between the fluids. However, second-order results tell a different story, and show that the viscosity contrast is crucial in determining the morphology of the interface. Our theoretical description is applicable to the entire range of viscosity contrasts, and provides insights on the formation of near-cusp pattern-forming structures. Reproduction of fully nonlinear, n -fold symmetric near-cuspidal shapes previously obtained through conformal mapping techniques substantiates the validity of our mode-coupling approach.

DOI: [10.1103/PhysRevE.103.063102](https://doi.org/10.1103/PhysRevE.103.063102)

I. INTRODUCTION

Complex pattern formation flourishes in nature and has been vigorously investigated in a number of physical, chemical, and biological systems [1–3]. In this broad field of scientific research, one chief point of interest is to try to understand the morphology of the patterns that emerge at the interface separating two different phases. In particular, the development of interfacial instabilities and patterns is an appealing problem in fluid dynamics. The study of pattern-forming structures arising in systems such as Taylor-Couette flow [4], Rayleigh-Bénard convection [5], and Rayleigh-Taylor instability [6] has motivated numerous experimental and theoretical works.

An important example of interfacial pattern formation in fluid systems is the Saffman-Taylor (or viscous fingering) problem [7], which occurs when a fluid displaces another of higher viscosity between the narrowly spaced plates of a Hele-Shaw cell [8]. Typical experimental demonstrations of this instability [9–17] involve the injection or suction of a fluid at the center of a Hele-Shaw. In those experiments, the fluid-fluid interface expands (or shrinks) radially and finger-like deformations begin to develop. The dynamic evolution of the viscous fingers is described by an effectively two-dimensional (2D), gap-averaged Darcy’s law, which connects the fluid velocity to the pressure gradient. A linear stability analysis of the interface evolution equations reveals that the occurrence of Saffman-Taylor instability is highly dependent

on the viscosity contrast

$$A = \frac{\eta_2 - \eta_1}{\eta_2 + \eta_1}, \quad (1)$$

where η_2 (η_1) denotes the viscosity of the outer (inner) fluid, and $-1 \leq A \leq 1$. In particular, it is found that for the Saffman-Taylor problem under injection (suction), the interface is unstable only for $A > 0$ ($A < 0$).

Curiously, the equivalent injection and suction pattern-forming problems for 2D Stokes flow have received less attention [18–24]. A possible reason for this is the practical difficulty to implement a legitimate 2D Stokes flow experimentally. However, there are some interesting theoretical findings on the development of interfacial instabilities in 2D Stokes flow. Analytical and numerical solutions of the time-evolving 2D Stokes flow problem based on complex variable methods [18–24] show that an injection-driven expanding bubble (bubble of negligible viscosity displacing a viscous outer fluid) is stable. It has been found that a growing bubble will approach an expanding circle for later times. On the other hand, it has been shown that a suction-driven, contracting circular bubble is unstable to disturbances. These observations are true both in the presence, or (even) in the absence of surface tension. In the absence of surface tension, the solutions for the interface under suction will in general break down in a finite time, owing to the formation of cusp singularities on the bubble surface. In contrast, suction of a bubble under finite surface tension sets a timescale for which narrow structures (known as “almost-cups” or “near-cusps”) can develop. The greater the surface tension, the later the near-cusp will appear. Analogous results have been observed in Refs. [21,22] for the suction of a blob of viscous fluid surrounded by an outer fluid of negligible viscosity under 2D Stokes flow circumstances. The analytical and numerical results obtained

*r.brandao18@imperial.ac.uk

†gabrieldiascarvalho@outlook.com

‡jose.mirandant@ufpe.br

in Refs. [18–24] for the suction flow cases in which $A = 1$ (bubble) and $A = -1$ (blob) reveal the development of fully nonlinear, very orderly interface shapes consisting of perfectly symmetric n -fold patterns, where the edges meet in sharp, near-cusp fingered protrusions having equal lengths.

The most striking results achieved in Refs. [18–24] for 2D Stokes flow are not those related to the surface tension, but the ones pertaining the effects of the viscosity contrast. Although the complex variable calculations carried out in Refs. [18–22] are limited to extreme values of the viscosity contrast (i.e., $A = 1$ for the bubble problem, and $A = -1$ for the blob situation), their results demonstrate that, as opposed to the Saffman-Taylor case, the 2D Stokes instability for suction occurs independently of the sign of the viscosity contrast A between the fluids. Similar findings have also been obtained in the linear stability analyses of the 2D Stokes flow for suction performed in Refs. [22–24]. As a matter of fact, the analytical linear stability theory developed in Refs. [23,24] considers a whole range of values for the viscosity contrast (i.e., $-1 \leq A \leq 1$) but found that the linear dispersion relation (linear growth rate) is independent of the sign and magnitude of A . This is in stark contrast to what happens in the usual viscous fingering problem with suction [9] where the viscosity contrast plays a very important role already in the linear regime. As explained in Ref. [23] the destabilizing mechanism for suction in 2D Stokes flow has a purely kinematic origin: it is simply due to the radial variation of the inward base flow, which amplifies any inward bump.

In recent years, the rapid development of microfluidics [25], superhydrophobic surfaces [26], and interesting dynamical experiments in inhomogeneous lipid membranes [24] brought renewed interest in the theory and experiments of 2D Stokes flows [27,28]. In fact, it has been shown that the study of interfacial phenomena in 2D Stokes flow could shed light on the modeling of some practical applications involving the interplay of hydrodynamic and elastic forces in 2D systems, used to study the shape evolution of 2D capsules and vesicles in Stokes flow [29–32], and the growth of tumors [33,34]. One particularly interesting set of works on 2D Stokes flow has been recently published [35–37], wherein the authors designed an apparatus allowing a thin and uniform layer of viscous fluid to propagate between two tractionless surfaces. Owing to the absence of wall friction, the flow is vertically uniform and satisfies a radial planar Stokes flow. By conducting advanced time experiments [35] and linear stability theory [36] in this geometry, the authors showed that the interface between a (non-Newtonian) shear-thinning fluid displacing a lower-viscosity fluid can become unstable, revealing the formation of fingers exhibiting rectangular-shaped tips. The planar problem studied in Refs. [35,36] has been extended to a curved geometry environment in Ref. [37] where a similar 2D Stokes flow has been examined on the surface of a sphere. Moreover, as stated in Refs. [35–37], the 2D Stokes flow configuration they study is similar to flow in a Hele-Shaw apparatus, but with no-stress instead of no-slip boundary conditions along the plates of the cell. In addition, it was suggested in Ref. [37] that another way to experimentally realize a 2D Stokes flow with injection and suction is by using a Hele-Shaw setup formed by two superhydrophobic surfaces. This opens up the possibility to perform realistic

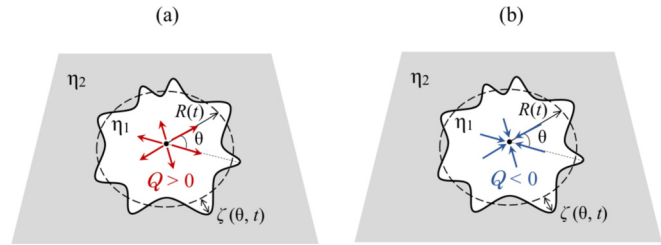


FIG. 1. A schematic of the 2D Stokes flow problem with (a) injection ($Q > 0$) and (b) suction ($Q < 0$), where Q is the areal rate. The outer (inner) fluid has viscosity η_2 (η_1). The time-dependent unperturbed fluid-fluid interface radius is represented by $R(t)$, and the interface perturbation is denoted by $\zeta(\theta, t)$, where θ is the azimuthal angle.

2D Stokes flow experiments using the well-known and vastly utilized Hele-Shaw cells, which certainly could help with the resurgence of practical interest in 2D Stokes flow.

Motivated by the new possibilities regarding experimental realizations of the 2D Stokes flow, and by the prospects of using it as a theoretical tool to examine a diverse spectrum of systems, in this work, we develop the weakly nonlinear analysis of the 2D Stokes flow with injection and suction. As we have already pointed out, existing analytical and numerical treatments of the problem describe the early and late time stages of the fluid-fluid interface, in the zero and small surface tension limits, mostly using conformal mapping techniques, or by employing boundary integral formulations. In addition, the majority of these studies focus on the cases in which the viscosity contrast is either $A = -1$ or $A = 1$, and just a few works address the effect of A (with $-1 \leq A \leq 1$) but are limited to the purely linear regime. Conversely, our work studies the intermediate stage between the linear and the fully nonlinear ones, focusing especially on the onset of nonlinear effects. Our approach applies to any value of surface tension and A , and gives insight into the mechanisms of cuspidal pattern formation in 2D Stokes flow. The linear stability analyses performed in Refs. [23,24,36] apply only to very early stages of the flow and do not offer ways to predict the morphological aspects of the essential cusp and near-cusp phenomena detected in later stages of the 2D Stokes flow. Here we show that a perturbative, second-order mode-coupling theory is able to address some of these issues and to investigate the role of A on the cusp-like shapes, an analysis which was not performed in previous studies. Comparison of our weakly nonlinear findings with fully nonlinear, highly symmetric pattern-forming structures previously obtained in Refs. [18,19,21,22] via conformal mapping techniques substantiates the validity of our perturbative mode-coupling approach.

II. BASIC EQUATIONS AND THE MODE-COUPLING APPROACH

Consider the 2D flow of a two-fluid system where an inner fluid 1 is surrounded by an outer fluid 2 (see Fig. 1). These fluids are viscous, Newtonian, immiscible, and incompressible. Note that the domain of fluid 2 is unbounded, extending to infinity in all directions, and the initial domain of fluid 1 is a circle of radius R_0 centered at the origin of the coordinate

system. Fluid 1 can be injected or sucked at the origin with a constant areal rate Q (area covered per unit time), which induces a radial flow. The cases of a single point source ($Q > 0$) and sink ($Q < 0$) correspond to injecting or sucking, respectively. In this framing, fluid flow is governed by the incompressible Stokes equations [38,39]

$$\nabla p_j = \eta_j \nabla^2 \mathbf{u}_j \quad (2)$$

and

$$\nabla \cdot \mathbf{u}_j = 0, \quad (3)$$

wherein η_j , p_j and \mathbf{u}_j denote the viscosity, pressure, and velocity fields of fluid j , with $j = 1(2)$ labels the inner (outer) fluid. Equation (2) is derived from the Navier-Stokes equation if one omits inertial terms (low Reynolds number limit), while Eq. (3) expresses the incompressibility of the fluids. Additionally, we assume that the interface between the fluids has a constant surface tension σ .

We parametrize the fluid-fluid interface by $r = \mathcal{R}(\theta, t)$, where (r, θ) are the usual polar coordinates centered at the injection (or suction) point, and define the unit normal and tangent vectors to the interface as

$$\hat{\mathbf{n}} = \frac{\mathcal{R}\hat{\mathbf{r}} - \frac{\partial \mathcal{R}}{\partial \theta} \hat{\boldsymbol{\theta}}}{\left[\mathcal{R}^2 + \left(\frac{\partial \mathcal{R}}{\partial \theta}\right)^2\right]^{1/2}}, \quad \hat{\mathbf{t}} = \frac{\frac{\partial \mathcal{R}}{\partial \theta} \hat{\mathbf{r}} + \mathcal{R}\hat{\boldsymbol{\theta}}}{\left[\mathcal{R}^2 + \left(\frac{\partial \mathcal{R}}{\partial \theta}\right)^2\right]^{1/2}}, \quad (4)$$

where $\hat{\mathbf{r}}$ ($\hat{\boldsymbol{\theta}}$) is the unit vector along the radial (azimuthal) direction. At the interface, we adopt the usual boundary conditions for 2D Stokes flow [18,23,38,39], for which velocity is continuous

$$\mathbf{u}_1 = \mathbf{u}_2, \quad (5)$$

where $\mathbf{u}_j = u_{r,j}\hat{\mathbf{r}} + u_{\theta,j}\hat{\boldsymbol{\theta}}$. The dynamic condition on the interface is obtained by considering the stress balance between the two fluids in both the normal and tangential directions. The balance equation of tangential stress is given by

$$\hat{\mathbf{n}} \cdot (\boldsymbol{\pi}_1 - \boldsymbol{\pi}_2)|_{\mathcal{R}} \cdot \hat{\mathbf{t}} = 0, \quad (6)$$

establishing the continuity of the shear stress. In addition, the normal stress balance equation gives

$$\hat{\mathbf{n}} \cdot (\boldsymbol{\pi}_1 - \boldsymbol{\pi}_2)|_{\mathcal{R}} \cdot \hat{\mathbf{n}} = -\sigma\kappa, \quad (7)$$

ensuring that the jump in the normal stress across the interface equals the product of the surface tension σ and the curvature of the interface κ . Since both fluids are assumed to be Newtonian, the stresses are related to pressure and velocity as [38,39]

$$\boldsymbol{\pi}_j = -p_j \mathbf{I} + \eta_j [\nabla \mathbf{u}_j + (\nabla \mathbf{u}_j)^T], \quad (8)$$

where \mathbf{I} is the identity matrix, and the superscript T denotes a matrix transpose. Moreover, since the interface is free, we impose a kinematic velocity condition relating the normal velocity on the interface to the interfacial deformation [12,18]

$$\frac{\partial \mathcal{R}}{\partial t} = \left(u_{r,j} - \frac{1}{r} \frac{\partial \mathcal{R}}{\partial \theta} u_{\theta,j} \right)_{r=\mathcal{R}}. \quad (9)$$

Equation (9) expresses the fact that the normal velocity of a point on the interface is equal to the normal component of fluid velocity at that point. It is based on the assumption that

the fluid-fluid boundary moves along with the fluid particles, coupling the motion of the interface to the motion of the bulk fluids.

During the injection or suction process, the initially unperturbed, circular interface can become unstable, and deform, due to the interplay of viscous and capillary forces. Within the scope of our perturbative mode-coupling scheme, we write the perturbed interface as $\mathcal{R}(\theta, t) = R(t) + \zeta(\theta, t)$, where

$$R(t) = \sqrt{R_0^2 + \frac{Q}{\pi} t} \quad (10)$$

is the time-dependent radius of the unperturbed interface, where $R(t=0) = R_0$. In addition, the net interface perturbation is Fourier expanded as

$$\zeta(\theta, t) = \sum_{n=-\infty}^{\infty} \zeta_n(t) \exp(in\theta), \quad (11)$$

where $\zeta_n(t)$ stands for the complex Fourier perturbation amplitudes, with integer wave numbers n . Note that our perturbative weakly nonlinear approach requires that $|\zeta(\theta, t)| \ll R(t)$. To ensure global mass conservation, the zeroth term of Eq. (11) is written in terms of the other modes as

$$\zeta_0(t) = -\frac{1}{R} \sum_{n \neq 0} |\zeta_n(t)|^2. \quad (12)$$

Note that the mode $n = 0$ corresponds to a dilation of a circular interface. It is also worth noting that in our 2D Stokes flow problem, there are some subtleties related to the Stokes paradox [40,41] for modes $n = \pm 1$. However, the modes $n = \pm 1$ correspond only to a translation (or, global off-center shift) of a circular interface, and since we focus on pattern formation of perturbed n -fold symmetric (noncircular) interfaces, this fact does not affect the generality of our problem. We stress that throughout this work our analysis is valid only for modes $n \neq 0, \pm 1$. Notice that this very same restriction on these mode numbers (i.e., $|n| \geq 2$) has been adopted in previous theoretical studies of the 2D Stokes flow problem [23,24].

Keep in mind that in this work we focus on the weakly nonlinear dynamic regime, and include terms up to second order in ζ . Existing linear stability analyses of the 2D Stokes flow problem [23,24,36] included only linear terms in ζ . Therefore, within such a linear approximation the Fourier modes decouple, so in the end the perturbation is restricted to a single mode. In contrast, our second-order weakly nonlinear approach considers the coupling of a full spectrum of Fourier modes. Although we are only at second order, mode interaction makes a big difference, allowing one to get useful information about the pattern's morphologies already at the lowest nonlinear level. In fact, the inclusion of the second-order perturbative terms is essential to properly capture and describe the underlying fingering process, in particular the emergence of the near-cusp structures [18–22]. Therefore, in this section, our primary aim is to derive a system of mode-coupling differential equations that describe the time evolution of the interfacial amplitudes $\zeta_n(t)$.

In our 2D Stokes flow problem, the base state corresponds to an expanding or retracting circular interface of radius given by Eq. (10), such that the associated velocity fields are just a

source or sink

$$\mathbf{u}_j^{(0)} = \frac{Q}{2\pi r} \hat{\mathbf{r}}, \quad (13)$$

where the superscript (0) denotes a base state solution. From Eqs. (2) and (3) we obtain that the base state pressures in the fluids are uniform and given by

$$p_1^{(0)} = \sigma \frac{1}{R} + \frac{(\eta_2 - \eta_1)Q}{\pi R^2}, \quad p_2^{(0)} = 0. \quad (14)$$

To obtain the velocities and pressures related to the perturbed interface evolution, as we did in Eq. (11) for the interface perturbation amplitudes, we need to write Fourier expansions for the pressure and velocity fields. In this way, we expand the pressure fields as

$$p_j = p_j^{(0)} + \sum_{n \neq 0, \pm 1} \tilde{p}_{n,j}(r, t) \exp(in\theta), \quad (15)$$

$$\frac{d^2 \tilde{b}_{n,j}}{dr^2} + \frac{3}{r} \frac{d\tilde{b}_{n,j}}{dr} + \frac{(1-n^2)}{r^2} \tilde{b}_{n,j} = (-1)^{j+1} \frac{|n|}{R} \frac{p_{j,n}}{\eta_j} \left(\frac{r}{R}\right)^{(-1)^{j+1}|n|-1}. \quad (20)$$

The solution of the above equation is

$$\tilde{b}_{n,j} = \frac{|n|}{|n| + (-1)^{j+1}} \frac{p_{n,j} R}{4\eta_j} \left(\frac{r}{R}\right)^{(-1)^{j+1}|n|+1} + b_{n,j} \left(\frac{r}{R}\right)^{(-1)^{j+1}|n|-1}. \quad (21)$$

Note that Eq. (21) is constituted by an inhomogeneous part, proportional to the pressure coefficients, and by a homogeneous part which depends on additional, yet undetermined, coefficients $b_{n,j}$.

To obtain the azimuthal velocity Fourier amplitudes in Eq. (17), we substitute Eq. (16) and Eq. (21) into the incompressibility condition [Eq. (3)], to get

$$\tilde{c}_{n,j} = i \frac{(-1)^{j+1}|n| + 2}{n} \frac{|n|}{|n| + (-1)^{j+1}} \frac{p_{n,j} R}{4\eta_j} \left(\frac{r}{R}\right)^{(-1)^{j+1}|n|+1} + i \frac{(-1)^{j+1}|n|}{n} b_{n,j} \left(\frac{r}{R}\right)^{(-1)^{j+1}|n|-1}. \quad (22)$$

For each Fourier mode n ($n \neq 0, \pm 1$), we must obtain four coefficients $p_{n,1}$, $p_{n,2}$, $b_{n,1}$ and $b_{n,2}$. To do that, we expand the boundary conditions given by Eqs. (5)–(7), the normal and tangent unit vectors in Eq. (4), retaining terms up to order ζ^2 ,

$$\hat{\mathbf{n}} \approx \left(1 - \frac{1}{2} \frac{\zeta_\theta^2}{R^2}\right) \hat{\mathbf{r}} - \frac{\zeta_\theta}{R} \left(1 - \frac{\zeta}{R}\right) \hat{\boldsymbol{\theta}} \quad \hat{\mathbf{t}} \approx \frac{\zeta_\theta}{R} \left(1 - \frac{\zeta}{R}\right) \hat{\mathbf{r}} + \left(1 - \frac{1}{2} \frac{\zeta_\theta^2}{R^2}\right) \hat{\boldsymbol{\theta}}, \quad (23)$$

and do the same for the curvature appearing in (7),

$$\kappa = \nabla \cdot \hat{\mathbf{n}} \approx \frac{1}{R} - \frac{1}{R^2} (\zeta + \zeta_{\theta\theta}) + \frac{1}{R^3} \left(\zeta^2 + \frac{1}{2} \zeta_\theta^2 + 2\zeta \zeta_{\theta\theta} \right). \quad (24)$$

Plugging Eqs. (15), (16), (17), (19), (21), and (22) into the boundary conditions, consistently expanding the equations up to the second order in ζ using Eqs. (23) and (24), and Fourier transforming, we arrive at an algebraic problem for the unknown coefficients. The considerably long expressions for the coefficients $p_{n,1}$, $p_{n,2}$, $b_{n,1}$, and $b_{n,2}$ are presented in the Appendix. By substituting these resulting expressions for the coefficients into the kinematic boundary condition [Eq. (9)], we finally obtain the equation of motion for the perturbation amplitudes (for $n \neq 0, \pm 1$)

$$\dot{\zeta}_n = \lambda(n) \zeta_n + \sum_{n' \neq 0, \pm 1} \mathcal{T}(n, n') \zeta_{n'} \zeta_{-n'}, \quad (25)$$

where the overdot represents a total time derivative, and

$$\lambda(n) = - \left[\frac{Q}{2\pi R^2} + \frac{\sigma}{2(\eta_1 + \eta_2)R} |n| \right] \quad (26)$$

the radial velocity fields as

$$u_{r,j} = \frac{Q}{2\pi r} + \sum_{n \neq 0, \pm 1} \tilde{b}_{n,j}(r, t) \exp(in\theta), \quad (16)$$

and the azimuthal velocity fields as

$$u_{\theta,j} = \sum_{n \neq 0, \pm 1} \tilde{c}_{n,j}(r, t) \exp(in\theta). \quad (17)$$

In the search for the mode-coupling equations for $\zeta_n(t)$, we proceed by taking the divergence of Eq. (2) and applying Eq. (3), to find that the pressure is harmonic

$$\nabla^2 p_j = 0. \quad (18)$$

Substituting the pressure expansion (15) into Laplace's equation (18), and Fourier transforming, yields

$$\tilde{p}_{n,j} = p_{n,j} \left(\frac{r}{R}\right)^{(-1)^{j+1}|n|}, \quad (19)$$

where $p_{n,j}$ are yet undetermined coefficients.

To determine the radial velocity Fourier amplitudes appearing in Eq. (16), we substitute Eq. (15) and Eq. (19) back into the radial component of Eq. (2), and take the Fourier transform, arriving at

denotes the linear growth rate. We note that the expression $\lambda(n)$ agrees with the linear dispersion relation in Refs. [23,24,36] within their respective regimes of validity. In addition, the second-order mode-coupling term is given by

$$\mathcal{T}(n, n') = -\frac{1}{2} \left(\frac{Q}{\pi R^3} \{A|n|\text{sgn}[n'(n - n')] - 1\} - \frac{\sigma}{2(\eta_1 + \eta_2)R^2} \{|n'| + |n - n'| - |n|\text{sgn}[n'(n - n')]\} \right), \quad (27)$$

with the sign function sgn being equal to ± 1 according to the sign of its argument. We note that the expression $\lambda(n)$ agrees with the linear dispersion relation in Refs. [23,24], when the latter is restricted to compressible fluids. Moreover, it also agrees with the results presented in Refs. [36] for Newtonian fluids in the absence of surface tension.

Equation (25), which is a central result of this work, is the mode-coupling equation of the 2D Stokes problem for injection and suction. This theoretical result contrasts with most findings obtained by previous analytical studies of the 2D Stokes flow with suction and injection which focused on investigating the problem via linear stability analysis [23,24,36]. The advantage of our weakly nonlinear approach over these previously reported linear studies is the possibility to assess intrinsically nonlinear interfacial behaviors related to the formation of the important near-cusp fingering structures, already at the lowest nonlinear order. Ordinarily, the study of such cusplike fingers has been performed at fully nonlinear dynamical stages of the evolution via conformal mapping and numerical simulations [18–22]. Another benefit of our weakly nonlinear approach is that, as opposed to these complex-variable-based numerical studies, our results are not restricted to the cases in which $A = \pm 1$, but can actually explore the whole range of allowed values of the viscosity contrast, i.e., $-1 \leq A \leq 1$. As a result, we can examine how A influences the overall shape of the cuspidal interfacial patterns in 2D Stokes flow. All these relevant issues will be discussed in Sec. III.

III. DISCUSSION

Prior to addressing the nonlinear aspects of the 2D Stokes problem under injection and suction which are related to the morphology of the pattern-forming structures, for the sake of clarity in Sec. III A we succinctly analyze certain fundamental features of the linear theory. This analysis is informative, and also useful for our subsequent weakly nonlinear investigation which is the main focus of our work, and will be performed in Secs. III B and III C.

A. Linear regime

We begin by discussing the linear growth rate expression given by Eq. (26). By inspecting the second term on the right-hand side of Eq. (26), one can readily see that, as usual, surface tension tends to stabilize interface disturbances. On the other hand, the first term on the right-hand side of Eq. (26) is somewhat peculiar. Notice that this term assumes positive values only in suction-driven flows, i.e., if $Q < 0$. Consequently, the interface is linearly unstable for suction, but stable for injection. Observe that this linear behavior for 2D Stokes flows is independent of the viscosity contrast A . As previously pointed out in Refs. [23,24,36], this last feature is in contrast

to what happens in the traditional viscous fingering (VF) problem in radial Hele-Shaw cells, where the linear dispersion relation is written as [9,12]

$$\lambda_{\text{VF}}(n) = \frac{Q}{2\pi R^2} (A|n| - 1) - \frac{\sigma b^2}{12(\eta_1 + \eta_2)R^3} |n|(n^2 - 1), \quad (28)$$

where b denotes the thickness of the Hele-Shaw cell. From the first term on the right-hand side of Eq. (28) it is evident that the viscosity contrast A has a key role in determining the linear stability of the interface. In the Darcy’s law regulated, radial viscous fingering problem, interfacial instability can occur for injection (suction) if $A > 0$ ($A < 0$). Therefore, irrespective of the sign of Q , the interface can deform only if the displacing fluid has smaller viscosity.

The linear growth rate for the 2D Stokes flow [Eq. (26)] is also unusual in another aspect: it decreases linearly with mode n , in such a way that the mode of maximum growth rate is

$$n_{\text{max}} = \pm 2, \quad (29)$$

corresponding to the smallest mode leading to interface deformation. Thus, assuming all modes to be initially present, and with comparable amplitudes, the resulting interface shape should exhibit only two lobes. However, an experimental realization of a 2D Stokes flow with suction in a biological system does not corroborate such an exotic linear prediction [24]. As a matter of fact, the establishment of a selection mechanism which determines the ultimate number of fingers formed in a 2D Stokes flows is still an open, and challenging, problem. There are some suggestions for such mode selection in the literature, but they are not consensual [23,24]. Nevertheless, in previous theoretical studies of the 2D Stokes flow problem, the symmetry of the interface was imposed through the initial conditions [18,19]. We note that experimentally “preparing” the initial conditions to have a certain symmetry is possible [42]. Note that the linear prediction for 2D Stokes flow expressed by Eq. (29) is also in contrast with the equivalent result for the radial viscous fingering case, in which the mode of maximum growth rate is obtained by setting $[d\lambda_{\text{VF}}(n)/dn]_{n=n_{\text{max}}^{\text{VF}}} = 0$, yielding

$$n_{\text{max}}^{\text{VF}} = \pm \sqrt{\frac{1}{3} \left[1 + \frac{6QAR(\eta_1 + \eta_2)}{\pi\sigma b^2} \right]}, \quad (30)$$

which is a time-dependent quantity since $R = R(t)$.

As indicated in some previous works [23,24,36,37], it is clear that the mechanism leading to interface destabilization in 2D Stokes flow is substantially different from the one responsible for triggering the Saffman-Taylor instability. As mentioned in Sec. I, it turns out that the instability mechanism in 2D Stokes flow is purely kinematic, and can be trivially understood [23]. For suction, the base flow (unperturbed) velocity is directed toward the origin, and its magnitude

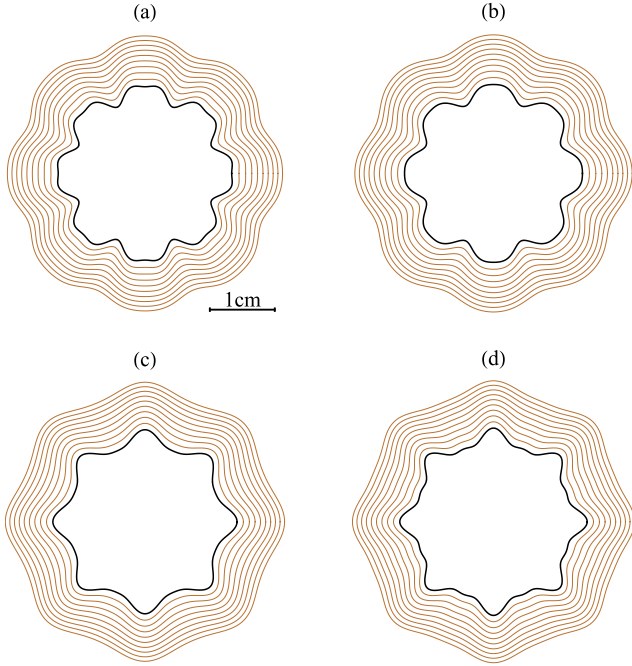


FIG. 2. Representative weakly nonlinear time evolution of the fluid-fluid interface for 2D Stokes flow with suction. The patterns are obtained by considering the coupling of two ($N = 2$) Fourier modes n , and $2n$. The values of the viscosity contrast are (a) $A = -1$, (b) $A = -0.5$, (c) $A = 0.5$, and (d) $A = 1$. The interfaces are plotted for times $48.8 \text{ s} \leq t \leq 49.7 \text{ s}$ in intervals of 0.1 s . The innermost interfacial pattern (taken at final time $t = t_f = 49.7 \text{ s}$) is highlighted, being represented by a thicker and darker curve. The horizontal bar in (a) indicates 1 cm .

increases as the interface radius decreases ($u_r \sim 1/r$). When the interface is perturbed away from a circle, points located closer to the origin are drawn radially inward more strongly than points farther from the origin. As a consequence, the interface tends to become more deformed. For injection, the opposite process takes place, and the interface tends to become more stable as it evolves outward.

A similar type of process is also present in the Saffman-Taylor instability problem. However, it constitutes only a secondary mechanism. The dominant mechanism for the onset of the Saffman-Taylor instability is the different viscous resistance of the two fluids at the walls of the Hele-Shaw cell. Thus, since the resistance depends on the fluids' viscosities, the usual viscous fingering instability is primarily dependent on the viscosity contrast. As commented in Sec. I, wall resistance is negligible in the 2D Stokes flow situation considered in this work. Thus, the viscosity contrast does not interfere in the linear stability of the interface. Nonetheless, as we will see in Secs. III B and III C the viscosity contrast A still substantially affects the interface morphology. To tackle these important morphological effects, one needs to go beyond the linear regime examined in Refs. [23,24,36] and explore the interface dynamics at the onset of the nonlinear stage of the evolution. Our lowest-order weakly nonlinear, mode-coupling approach is capable of capturing the most relevant aspects of the interface morphology in the 2D Stokes flow problem with suction.

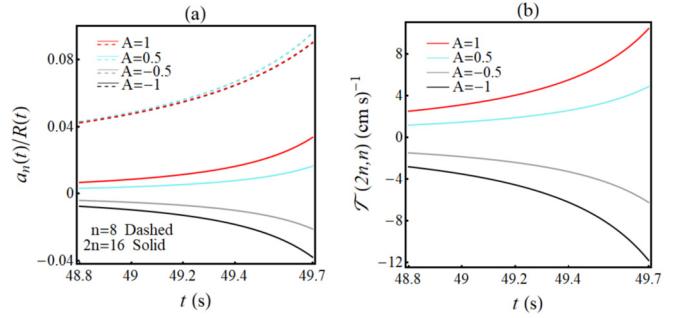


FIG. 3. (a) Time evolution of the rescaled cosine amplitudes $a_n(t)/R(t)$ for modes $n = 8$ (dashed curves) and $2n = 16$ (solid curves), corresponding to the interface evolutions depicted in Fig. 2, for four values of A (-1 , -0.5 , 0.5 , and 1). Note that hidden in each dashed curve in (a) there are in fact two curves. The curves for $A = \pm 1$ are indistinguishable. The same is true for the dashed curves for $A = \pm 0.5$. (b) Variation of the function $\mathcal{T}(2n, n)$ with time, related to the growth of the first harmonic mode $2n$ as given in Eqs. (32) and (33). As in Fig. 2, in both (a) and (b) we have that $48.8 \text{ s} \leq t \leq 49.7 \text{ s}$.

B. Weakly nonlinear stage

We initiate our discussion about the weakly nonlinear regime of the 2D Stokes by calling the readers' attention to a very important point. If on one hand, it is true that the linear growth rate $\lambda(n)$ [Eq. (26)] does not depend on the viscosity contrast A , on the other hand, it is also a fact that the second-order mode-coupling function $\mathcal{T}(n, n')$ [Eq. (27)] does depend on A . The verification that such an important dependence on A arises already at the lowest nonlinear level is promising. It opens up the possibility of investigating the role played by A in determining the shape of the interfacial patterns already at second order. As discussed in Sec. III A, in the 2D Stokes flow problem the interface is linearly stable for the case of injection ($Q > 0$). As a matter of fact, we have verified that under injection the interface remains stable against perturbations for all modes $|n| \geq 2$ during the weakly nonlinear stage of the flow. In these circumstances, the nonlinear behavior of the expanding interface is not exactly interesting, as it grows axisymmetrically as a stable circular front. For this reason, throughout the rest of this work our major purpose is to use the mode-coupling equations (25)–(27) to obtain perturbative solutions for the 2D Stokes flow interfacial patterns in the case of suction ($Q < 0$).

By considering the coupling of a finite number of participating Fourier modes, we aim to extract the most important morphological features of the emerging patterns, and possibly get perturbative pattern-forming structures resembling the highly symmetric, n -fold near-cusp fingering shapes obtained in Refs. [18–22]. Recall that in previous works such symmetrical almost-cusp shapes have been accessed via exact solutions, or numerical simulations based on conformal mapping techniques. In addition, contrary to studies based on conformal mappings, whose results are restricted to cases in which $A = -1$ or $A = 1$, our mode-coupling theory can address a whole range of allowed values for the viscosity contrast, i.e., $-1 \leq A \leq 1$. Another advantage of our scheme

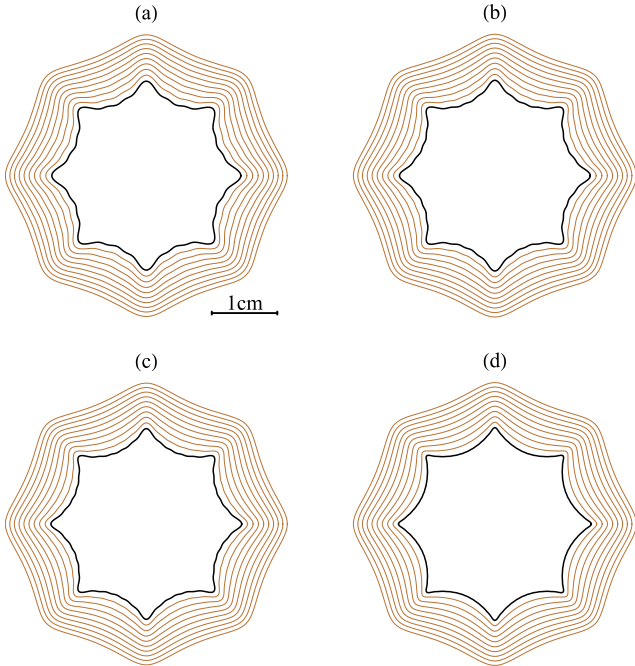


FIG. 4. Weakly nonlinear evolution of the 2D Stokes flow patterns for viscosity contrast $A = 1$. These patterns are generated by using an increasingly larger number of participating modes N : (a) 3, (b) 4, (c) 5, and (d) 10. The innermost interfacial pattern (taken at final time $t = t_f = 49.7$ s) is highlighted, being represented by a thicker and darker curve. The horizontal bar in (a) indicates 1 cm.

is the fact that it is perturbative on the interface deformation ζ , but nonperturbative on the surface tension σ .

With the second-order mode-coupling equation for the complex amplitudes (25) at hand, it is relatively simple to obtain the time evolution of the fluid-fluid interfaces. To generate the perturbative 2D Stokes flow patterns, we consider the nonlinear coupling of a finite number N of Fourier modes. Based on the symmetry properties of the fully nonlinear n -fold structures having near-cusp fingers of equal sizes obtained in Refs. [18–22] via conformal mapping techniques, we consider the coupling of a fundamental mode n and its harmonics $2n, 3n, \dots, Nn$, and rewrite Eq. (25) in terms of the real-valued cosine amplitudes $a_n(t) = \zeta_n(t) + \zeta_{-n}(t)$ to obtain

$$\dot{a}_n = \lambda(n)a_n + \frac{1}{2} \sum_{n' > 2} [\mathcal{T}(n, -n')a_{n'}a_{n+n'} + \mathcal{T}(n, n')a_{n'}a_{n-n'}]. \quad (31)$$

Equations (31) are the mode-coupling ordinary differential equations for the time evolution of the cosine mode amplitudes, accurate to second order. Then the growing patterns are generated by numerically solving the corresponding coupled nonlinear differential equations for the mode amplitudes $a_n(t)$. Once this is done, the shape of the interface is found by utilizing Eq. (11). In addition, to make sure that the interfacial behaviors we detect are spontaneously induced by the weakly nonlinear dynamics, and not by artificially imposing large initial amplitudes for the harmonic modes, we always set the initial ($t = 0$) harmonic mode amplitudes to zero, i.e., $a_{2n}(0) = a_{3n}(0) = \dots = a_{Nn}(0) = 0$. Therefore, at $t = 0$ only

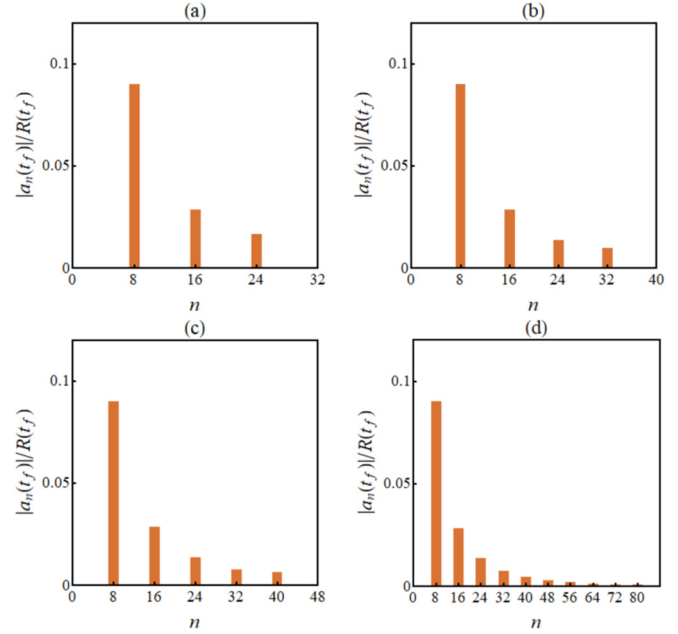


FIG. 5. Rescaled cosine mode amplitudes $|a_n(t)|/R(t)$ taken at the final time $t = t_f$, as a function of the azimuthal mode number n , when (a) $N = 3$, (b) $N = 4$, (c) $N = 5$, and (d) $N = 10$. The data represented by the vertical bars are extracted from the corresponding patterns that appear in Fig. 4. Note that for the largest amplitude (mode $n = 8$) we have that $a_8(t_f) \approx 9\%$ of $R(t_f)$.

the fundamental mode n has a nonzero, but small amplitude $a_n(0)$. This is done to avoid artificial growth of the harmonic modes, imposed solely by the initial conditions.

In order to strengthen the practical and academic relevance of our weakly nonlinear results, throughout this work we use typical parameter values for all physical quantities that are in line with the ones utilized in existing experimental and theoretical studies for the equivalent problem in radial Hele-Shaw cells [9–16]. Therefore, it should be clear that the set of physical parameters we use here is quite representative of other values commonly utilized in many other radial Hele-Shaw cell experiments. In this way, in the various situations analyzed in this work we consider that the viscosities of the fluids may vary within the range $0 \leq \eta_j \leq 10$ g/cm s. The suction rate is taken as $Q = -9$ cm²/s, and the surface tension between the fluids is $\sigma = 0.6$ dyne/cm. In addition, we evolve from the initial radius $R_0 = 12$ cm, and consider the initial amplitude of the fundamental mode as $a_n(0) = R_0/150$ cm. In Figs. 2–7 we take, without loss of generality, the fundamental mode as $n = 8$. The effect of considering a different value for the fundamental n on the resulting patterns will be discussed at the end of this section, in the analysis of Fig. 8. Finally, we point out that in all calculations and plots presented in this work, we paid close attention to the limit of validity of our perturbative theory, in such a way that we always make sure that $|\zeta_n(t)| \ll R(t)$. The reliability of our second-order mode-coupling approach will be discussed in Sec. III C. There we perform a quantitative comparison between our weakly nonlinear patterns with the corresponding fully nonlinear shapes computed in Refs. [18, 19, 22] through complex variable methods.

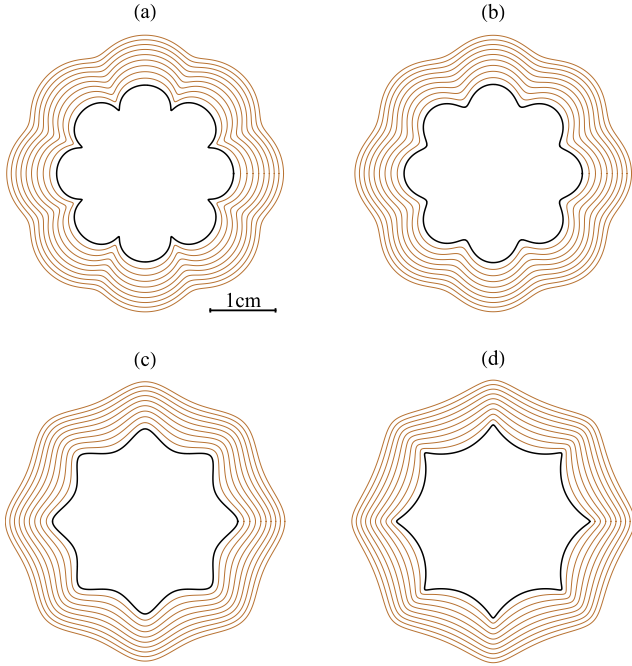


FIG. 6. Representative weakly nonlinear time evolution of the fluid-fluid interface for 2D Stokes flow with suction. The patterns are obtained by considering the coupling of 60 participating modes ($N = 60$). The values of the viscosity contrast are (a) $A = -1$, (b) $A = -0.5$, (c) $A = 0.5$, and (d) $A = 1$. As customary, the innermost interfacial pattern (taken at final time $t = t_f = 49.7$ s) is highlighted, being represented by a thicker and darker curve. The horizontal bar in (a) indicates 1 cm.

We initiate our analysis by examining the simplest second-order scenario, and consider the interplay of only two Fourier modes ($N = 2$): the fundamental $n = 8$, and its first harmonic $2n = 16$. The choice of using precisely these modes (the fundamental n , and its first harmonic $2n$) to begin our investigation can be justified as follows. Remember that an emblematic feature of the bubble ($A = 1$) and blob ($A = -1$) shape solutions obtained via complex variable techniques in Refs. [18–22] is the formation of regular, n -fold polygonal-

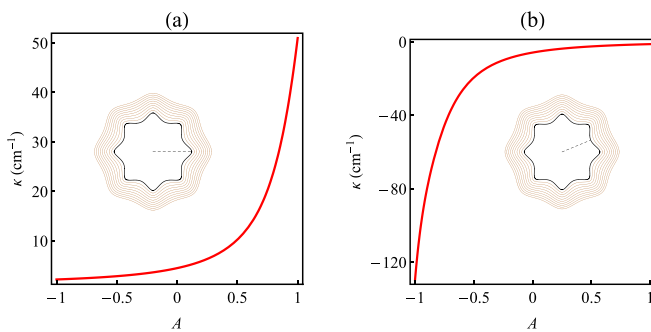


FIG. 7. Behavior of the interface curvatures κ as the viscosity contrast A is varied from -1 to 1 , for two specific angular locations: (a) $\theta = 0$, and (b) $\theta = \pi/8$. To guide the eye, the dashed lines in the insets locate these angles for the pattern depicted in Fig. 6(c) for $A = 0.5$. Here κ is computed at the final time $t = t_f = 49.7$ s as in Fig. 6.

like interfaces having sharp, cusplike fingers. It turns out that a two-mode mode-coupling approach is quite appropriate to examine pattern-forming mechanisms involving the growth of sharp fingering structures. It has been shown that finger-tip sharpening, widening, and splitting are behaviors related to the influence of a fundamental mode n on the growth of its harmonic mode $2n$ [12]. In fact, within the scope of mode coupling, these basic pattern formation phenomena can be predicted, captured and properly described already at second order in the perturbation amplitudes.

The occurrence of these types of finger tip phenomena in 2D Stokes flow with suction can be examined by considering the mode-coupling equation (31) for cosine mode amplitudes, and analyzing the influence of a fundamental mode n on the growth of its harmonic $2n$. In this situation, the equation of motion for the growth of the harmonic mode amplitude can be written as

$$\dot{a}_{2n} = \lambda(2n)a_{2n} + \frac{1}{2}\mathcal{T}(2n, n)a_n^2, \quad (32)$$

where

$$\mathcal{T}(2n, n) = -\left[\frac{Q}{\pi R^3}\left(A|n| - \frac{1}{2}\right)\right]. \quad (33)$$

Likewise, the equation of motion for the growth of the fundamental mode amplitude is

$$\dot{a}_n = \lambda(n)a_n + \frac{1}{2}[\mathcal{T}(n, -n) + \mathcal{T}(n, 2n)]a_n a_{2n}, \quad (34)$$

where the functions $\mathcal{T}(n, -n)$ and $\mathcal{T}(n, 2n)$ can be readily obtained from Eq. (27).

It turns out that [12] that the most relevant information about the finger tip morphology (tip sharpening or tip widening) can be extracted from Eqs. (32), (33), and (34). Note that the mode-coupling function $\mathcal{T}(2n, n)$ in Eq. (33) assumes a very simple form that depends on the viscosity contrast A . The interesting point about the function $\mathcal{T}(2n, n)$ is that it controls the finger shape behavior, and ultimately the morphology of the resulting pattern. The sign of $\mathcal{T}(2n, n)$ dictates whether finger tip-sharpening or finger tip widening is favored by the dynamics. From Eq. (32) we see that if $\mathcal{T}(2n, n) > 0$, the result is a driving term of order a_n^2 forcing growth of $a_{2n} > 0$, the sign that is required to cause inward-pointing fingers to become wide, favoring finger tip-broadening. In contrast, if $\mathcal{T}(2n, n) < 0$ growth of $a_{2n} < 0$ would be favored, leading to inward-pointing finger tip sharpening.

To further investigate the analytic predictions for the finger tip shape behavior provided by Eqs. (32) and (33), in Fig. 2 we plot representative 2D flow patterns generated by considering the coupling of modes $n = 8$ and $2n = 16$. This is done for four values of the viscosity contrast: (a) $A = -1$ ($\eta_1 = 10$ g/cm s and $\eta_2 = 0$); (b) $A = -0.5$ ($\eta_1 = 7.5$ g/cm s and $\eta_2 = 2.5$ g/cm s); (c) $A = 0.5$ ($\eta_1 = 2.5$ g/cm s and $\eta_2 = 7.5$ g/cm s); and (d) $A = 1$ ($\eta_1 = 0$ and $\eta_2 = 10$ g/cm s). The interfaces are plotted for times 48.8 s $\leq t \leq 49.7$ s in intervals of 0.1 s. Note that while varying the values of the viscosity contrast A , we keep the sum $\eta_1 + \eta_2$ fixed in order to maintain the linear growth rate (25) unchanged as A is modified. These very same values of A , and times will be used to plot Figs. 4 and 6. By inspecting Fig. 2 it is clear that the inward-moving interface becomes increasingly unstable as time progresses. One interesting point is that, despite the fact that the linear

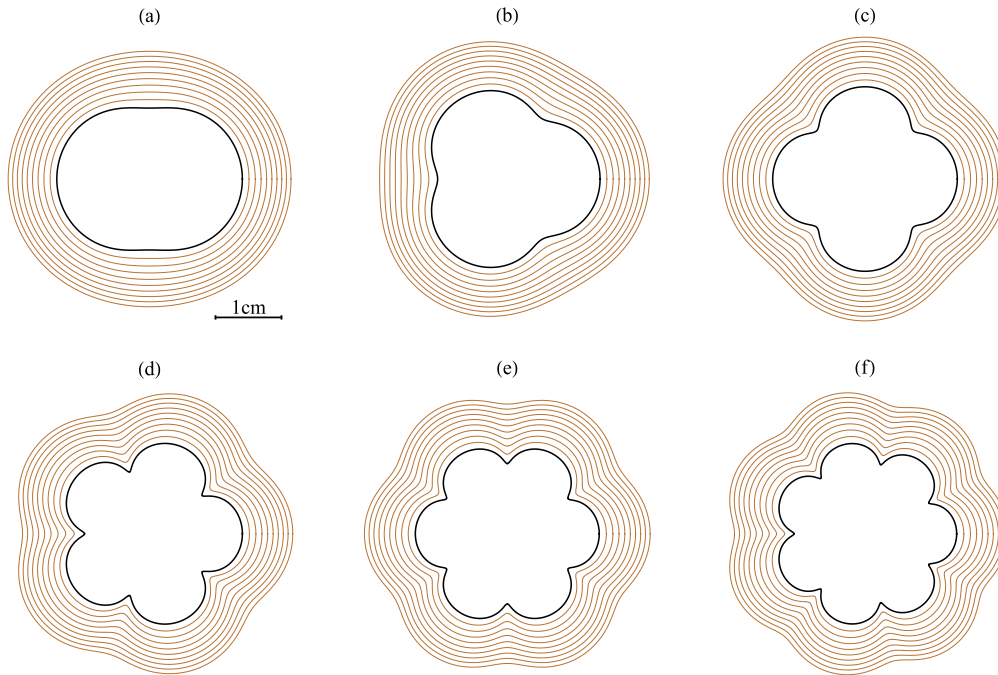


FIG. 8. Representative weakly nonlinear time evolution of the interface for 2D Stokes flow with suction, with viscosity contrast $A = -1$. The patterns are obtained by considering that the fundamental mode, and its initial amplitude are taken as (a) $n = 2$, and $a_n(0) = R_0/450$ cm; (b) $n = 3$, and $a_n(0) = R_0/350$ cm; (c) $n = 4$, and $a_n(0) = R_0/280$ cm; (d) $n = 5$, and $a_n(0) = R_0/210$ cm; (e) $n = 6$, and $a_n(0) = R_0/210$ cm; and (f) $n = 7$, and $a_n(0) = R_0/180$ cm. All the other parameters are identical to those used in Figs. 2–7. In (a)–(f) the innermost interfacial pattern is highlighted, being represented by a thicker and darker curve. The horizontal bar in (a) indicates 1 cm. In (a)–(f) the largest mode amplitudes at $t = t_f$, $a_n(t_f)$, vary from $\approx 9.5\%$ of $R(t_f)$ to $\approx 13\%$ of $R(t_f)$.

growth rate $\lambda(n)$ does not depend on A , the morphology of the final weakly nonlinear patterns (represented by the innermost interfaces in Fig. 2) do depend on the value A . Note that if $A < 0$ (or, if $\mathcal{T}(2n, n) < 0$) [Figs. 2(a) and 2(b)] one observes the formation of inward-moving fingers that are sharp, while the structures separating these sharp fingers look blunt [Fig. 2(b)] or split into two small protuberances [Fig. 2(a)]. The opposite behavior is observed if $A > 0$ [or, if $\mathcal{T}(2n, n) > 0$] [Figs. 2(c) and 2(d)] where the inward-moving finger looks wider (or even split at their tips), while the structures separating consecutive wide fingers look sharp. Of course, these pictorial observations are in agreement with the analytical predictions provided by our discussion of Eqs. (32) and (33), as further clarified in Fig. 3.

Figure 3(a) shows the time evolution of the rescaled cosine amplitudes $a_n(t)/R(t)$ for the fundamental mode $n = 8$ (dashed curves) and its first harmonic $2n = 16$ (solid curves), corresponding to the interface evolutions portrayed in Fig. 2, for four representative values of the viscosity contrast A : $-1, -0.5, 0.5$, and 1 . As in Fig. 2, in Fig. 3 one has that $48.8 \text{ s} \leq t \leq 49.7 \text{ s}$. By observing Fig. 3(a), it is evident that while the evolution of the mode amplitudes $a_8(t)/R(t)$ (that set the overall eightfold symmetry of the pattern) are not very sensitive to changes in A , the growth of $a_{16}(t)/R(t)$ (that determine finger tip narrowing and widening behaviors) are significantly affected as A is varied. Figure 3(b) shows how the function $\mathcal{T}(2n, n)$ [connected to the growth of the first harmonic mode as given in Eqs. (32) and (33)] varies with time, for $A = -1, -0.5, 0.5$, and 1 . It demonstrates very vividly that the growth of the first harmonic amplitudes $a_{16}(t)/R(t)$

(their magnitudes and signs) in Fig. 3(a) is determined by the function $\mathcal{T}(2n, n)$, and consequently by A .

By examining Fig. 2 we also note that as the viscosity contrast varies from $A = -1$ to $A = 1$, the tips of the inward-moving fingers located at polar angle $\theta = \pi/8$ tend to become wider, while the interface point located at angle $\theta = 0$ tends to get locally sharper. In this sense, our two mode second-order mimic of the pattern formation dynamics indicates that sharp fingers pointing inward should arise at $\theta = \pi/8$ in the blob case ($A = -1$), while sharp structures pointing outward should appear at $\theta = 0$ in the bubble case ($A = 1$). These last observations are reassuring in the sense that they are in qualitative agreement with what has been observed in Refs. [18–22] regarding the formation of near-cusps. However, the weakly nonlinear patterns depicted in Fig. 2 are still very different from the cusped interfaces generated in Refs. [18–22].

In the pursuit of getting a closer morphological similarity between our weakly nonlinear patterns, and the fully nonlinear cusplike shapes obtained in Refs. [18–22], we pass to consider the coupling of an increasingly larger number N of participating Fourier modes. This is done in Fig. 4, where we investigate the influence of the number of participating Fourier modes in determining the shape of the 2D Stokes flow patterns at second order. In Fig. 4 we focus on the case in which $A = 1$, and produce patterns using the coupling of modes $n, 2n, \dots, Nn$, where $n = 8$ is the fundamental mode: (a) $N = 3$, (b) $N = 4$, (c) $N = 5$, and (d) $N = 10$. It should be noted that all other physical quantities and initial conditions are exactly the same as those used in Fig. 2.

By going through Fig. 4, it is apparent that the consideration of a larger number of interacting Fourier modes leads to promising results. The weakly nonlinear patterns portrayed in Fig. 4 reveal the formation of symmetric, eightfold polygonal-like morphologies (set by the fundamental mode) having concave-shaped edges. These edges present small undulations determined by the number of participating modes N . Since the fluid-fluid interface is not discontinuous, no Gibbs phenomenon [43] is present, and the Fourier series converges. Therefore, as N is increased, the amplitude of the oscillations decreases, and the edges of the polygonal patterns look increasingly smoother. This is clearly illustrated by Figs. 4(a)–4(d). Eventually, for a sufficiently large N these oscillations are no longer observed. It is also noticeable that the vertices of the patterns become sharper as N is augmented. Finally, it is worthwhile to note that the weakly nonlinear pattern depicted in Fig. 4(d) for $N = 10$ bears a close resemblance to the typical fully nonlinear, near-cusp shapes obtained by Tanveer and Vasconcelos for the case $A = 1$ via complex variable methods in Refs. [18,19]. Although the discussion of Fig. 4 focuses on the case in which $A = 1$, similar types of results related to the role of increasingly larger N 's are also found for all allowed values of A .

Complementary information about the pattern-forming structures illustrated in Fig. 4 is provided by Fig. 5, which plots the absolute value of the cosine Fourier amplitudes $|a_n(t)|$, rescaled by the unperturbed radius of the interface $R(t)$ (given by the vertical bars), at the final time $t = t_f = 49.7$ s, for various participating modes n . From the Fourier spectra shown in Fig. 5 it is evident that the cosine mode amplitudes drop very quickly as n is increased. Despite this quick drop, the Fourier series does not converge as rapidly, and the consideration of a greater number of modes is necessary to make the edges of the polygonal patterns to become sufficiently smooth.

Inspired by the findings of Fig. 4 and Fig. 5, in Fig. 6 we display a representative set weakly nonlinear 2D Stokes flow patterns with suction, now using a sufficiently large number of participating modes ($N = 60$) in such a way that the edges of the polygonal-like patterns are quite smooth. Similar to what we did in Fig. 2, the patterns displayed in Fig. 6 are obtained for four representative values of the viscosity contrast: (a) $A = -1$, (b) $A = -0.5$, (c) $A = 0.5$, and (d) $A = 1$. All the rest of the physical parameters and initial conditions are equal to the ones used in Fig. 2. Figure 6 is quite elucidating since it allows one to visualize the impact of the viscosity contrast A on the shape of the emerging patterns, already at the lowest nonlinear level. For example, the weakly nonlinear pattern shown in Fig. 6(a) for $A = -1$ reveals the most salient features encountered in the complex-variable-generated shapes obtained for the sucking of a blob of fluid (see, for instance, Fig. 3 in Ref. [22]). In Fig. 6(a) we have an eightfold polygonal-like morphology, now having convex-shaped edges that meet at near-cusp, inward-pointing indentations (see, for example, the near-cusp formed at $\theta = \pi/8$). On the other hand, when $A = -0.5$ [Fig. 6(b)] no near-cusp indentations are found, and the inward-pointing fingers are not that sharp.

In addition, when $A = 0.5$ [Fig. 6(c)] yet another type of pattern arises: it has a starfishlike shape, and also does not show any signs of near-cusp formation. By contrasting the finger shapes in illustrated in Figs. 6(b) and 6(c), one sees

that while the fingering structures formed at $\theta = \pi/8$ become more rounded and wider, the ones produced at $\theta = 0$ tend to become sharper and narrower. This trend persists when we look at the pattern portrayed in Fig. 6(d) for $A = 1$: in $\theta = \pi/8$ the fingering structure has a near-circular shape, whereas in $\theta = 0$ a near-cusp, outward-pointing finger is unveiled. As anticipated by the structure obtained in Fig. 4(d) for $N = 10$, the pattern displayed in Fig. 6(d) for $N = 60$ is indeed an eightfold polygonal-like interface, but now it has smooth, concave-shaped edges. Incidentally, the weakly nonlinear structure represented in Fig. 6(d) does have all essential morphological elements of the typical symmetric shapes obtained for the sucking of a bubble in Refs. [18,19] (see, for instance, Fig. 4 in Ref. [18], and Fig. 1 in Ref. [19]). In Sec. III C we make a more quantitative comparison of our weakly nonlinear cusped interfaces depicted in Fig. 6 for $A = \pm 1$ with the equivalent fully nonlinear structures obtained via complex variable techniques in Refs. [18,19,21,22].

By analyzing Fig. 6(a) for $A = -1$, and Fig. 6(d) for $A = 1$, it is interesting to note that regardless of whether the near-cusps point inward ($A = -1$) or outward $A = 1$, they always occur in the direction pointing from the less viscous fluid to the more viscous one. This indicates that the near-cusp phenomenon is determined by a viscosity difference mechanism present in the nonlinear terms of the dynamics [note the presence of A in Eq. (27)] which clearly manifests itself for extreme values of the viscosity contrast ($A = \pm 1$).

To better substantiate the impact of the viscosity contrast A on the morphologies of the 2D Stokes flow patterns for a whole range of values of A , in Fig. 7 we plot the value of the interface curvatures κ at the final time $t = t_f = 49.7$ s, as A is varied from $A = -1$ to $A = 1$, for points positioned at two important angular locations along the interface: (a) at $\theta = 0$, and (b) $\theta = \pi/8$. The interface curvature can be readily calculated from Eq. (24). Note that the rest of the parameters and initial conditions used in Fig. 7 are equal to those utilized in Fig. 2. By observing Fig. 7(a) we see that the interface curvature at $\theta = 0$ is relatively small for negative values of A , and then starts to grow very significantly as A varies from 0 to 1, reaching a maximum value at $A = 1$, where a near-cusp fingered structure is formed. Note that in (a) $\kappa > 0$ meaning the fingers at $\theta = 0$ point outward. On the other hand, in Fig. 7(b) we verify that at $\theta = \pi/8$, the curvature is very high and negative for $A = -1$ where an inward-pointing near-cusp finger arises, and then becomes much less intense as the viscosity contrast changes from $A = -1$ to $A = 0$, until assuming considerably small negative values as $A \rightarrow 1$. Observe that these quantitative remarks about the behavior of κ with A in Fig. 7 are in accordance with the more visual verifications one can make at angles $\theta = 0$ and $\theta = \pi/8$ in the patterns depicted in Fig. 6. The dramatic variation of κ with A illustrated in Fig. 7 reinforces the importance of the viscosity contrast in determining the overall morphology of the pattern-forming structures in our problem.

We close this section by discussing the effect of considering a different value for the fundamental mode n on the generated 2D Stokes flow, weakly nonlinear patterns with suction. In Figs. 2–7, we took $n = 8$. As mentioned earlier in this work, the choice of $n = 8$ as the fundamental mode was made without loss of generality. It turns out that $n = 8$ is a

linearly unstable mode for the time interval used in Figs. 2–7. If one chooses another linearly unstable Fourier mode as being the fundamental mode, the basic physical results are similar to the ones obtained for $n = 8$. This is illustrated in Fig. 8 which shows suction patterns produced for viscosity contrast $A = -1$, by taking different values for the fundamental mode and its initial amplitude, namely, for (a) $n = 2$, and $a_n(0) = R_0/450$ cm; (b) $n = 3$, and $a_n(0) = R_0/350$ cm; (c) $n = 4$, and $a_n(0) = R_0/280$ cm; (d) $n = 5$, and $a_n(0) = R_0/210$ cm; (e) $n = 6$, and $a_n(0) = R_0/210$ cm; and (f) $n = 7$, and $a_n(0) = R_0/180$ cm. Other than that, these patterns are generated by utilizing all the physical parameters used in Figs. 2–7. By scrutinizing Fig. 8 one readily observes that the types of pattern-forming structures obtained when $A = -1$ for these modes of lower wave number than $n = 8$ are morphologically similar to the corresponding structure shown in Fig. 6(a) when $n = 8$ and $A = -1$. In other words, all these structures for $A = -1$ and different n have a characteristic polygonal-like morphology, having convex-shaped edges that can meet at near-cusps, inward-pointing dents. We have verified that the behavior exemplified in Fig. 8 for the case $A = -1$ as n is changed, also occurs for all other values of A .

C. Weakly nonlinear versus fully nonlinear results

To confirm the validity of our weakly nonlinear mode-coupling scheme in a more quantitative fashion, in this section we compare our perturbative solutions for the fluid-fluid interface in the 2D Stokes flow problem with suction with their fully nonlinear counterparts that have been investigated previously in the literature. The studies performed in Refs. [18,19,21,22] rely on complex function theory and mapping techniques to determine the dynamics of the interface, and present a general class of exact solutions for a time-evolving bubble ($A = 1$), or blob ($A = -1$). These elegant conformal mapping, time-dependent solutions are able to describe the fully nonlinear dynamics of a contracting interface in the extreme cases $A = \pm 1$, for which near-cusps structures can be detected. Below, we briefly present how these conformal mapping solutions for the situations $A = \pm 1$ are obtained, and contrast them with the corresponding second-order perturbative solutions we derived in this work.

Within the conformal mapping approach, for the case $A = -1$, only the inner fluid needs to be considered. It was shown

$$I_+(u_+, v_+) = \frac{1}{2\pi} \int_0^\pi \frac{d\omega}{[u_+^2 + (m-1)v_+^2 - 2(m-1)u_+v_+ \cos m\omega]^{1/2}}. \tag{42}$$

We continue by examining Fig. 9, which compares our second-order, weakly nonlinear (WNL) solutions for the cases (a) $A = 1$, (b) $A = -1$, considering 60 participating modes ($N = 60$), with the corresponding eightfold symmetric ($m = 8$) fully nonlinear solutions of the problem, obtained by solving Eqs. (35) and (39) numerically. The top panels in Fig. 9 contrast the WNL interfaces [represented by the solid curves, and obtained from the numerical solution of the mode-coupling Eqs. (31)], with the corresponding fully nonlinear

in Ref. [21] that the flow in the inner fluid domain can be conformally mapped into the flow inside the unit circle. In detail, we parametrize the domain of the inner fluid by $z = re^{i\theta}$ with $r \leq \mathcal{R}(t)$ and the interior of the unit circle by $\xi = \rho e^{i\varphi}$ with $\rho \leq 1$ and $0 \leq \varphi < 2\pi$. Note that $r = \mathcal{R}$ is mapped to $\rho = 1$. For an interfacial pattern with m th-fold symmetry, where $m > 1$, the mapping derived in Ref. [21] assumes the form

$$z = u_-(t)\xi + v_-(t)\xi^{m+1}, \tag{35}$$

where the time-dependent coefficients satisfy

$$u_-^2 + (m+1)v_-^2 = \frac{A_0 + Qt}{\pi} \tag{36}$$

and

$$\dot{v}_- = -\frac{v_-}{u_-^2 - (m+1)v_-^2} \left[\frac{Q}{2\pi} + m \frac{\sigma}{\eta_1} u_-^2 I_-(u_-, v_-) \right], \tag{37}$$

with A_0 being the initial area occupied by the inner fluid and

$$I_-(u_-, v_-) = \frac{1}{2\pi} \int_0^\pi \frac{d\omega}{[u_-^2 - (m+1)v_-^2 \cos \omega]^{1/2}}. \tag{38}$$

On the other hand, for the situation in which $A = 1$, only the outer fluid needs to be considered, and an analogous conformal mapping can be employed to analyze this case [18,19]. We parametrize the domain of the outer fluid by $z = re^{i\theta}$ with $r \geq \mathcal{R}(t)$ and parametrization of the interior of the unit circle is the same as before, with $r = \mathcal{R}$ corresponding to $\rho = 1$. For a fluid-fluid interface with m th-fold symmetry, with $m > 1$, the mapping derived in Refs. [18,19] assumes the form

$$z = \frac{u_+(t)}{\xi} + v_+(t)\xi^{m-1}, \tag{39}$$

where

$$u_+^2 - (m-1)v_+^2 = \frac{A_0 + Qt}{\pi} \tag{40}$$

and

$$\dot{v}_+ = -\frac{v_+}{u_+^2 + (m-1)v_+^2} \left[\frac{Q}{2\pi} + m \frac{\sigma}{\eta_2} u_+^2 I_+(u_+, v_+) \right], \tag{41}$$

with

solutions of the problem, [represented by dashed curves, and obtained via solution of Eqs. (35) and (39)]. Note that the eightfold WNL pattern portrayed in Fig. 9(a) [Fig. 9(b)] was originally illustrated in Fig. 6(d) [Fig. 6(a)]. However, in order to facilitate the visualization of the morphological details of the resulting pattern-forming structures, in Fig. 9 instead of plotting the entire patterns (for $0 \leq \theta \leq 2\pi$) as in Fig. 6, the top panels of Fig. 9 depict just a close-up views of part of the patterns (for the angular sector $0 \leq \theta \leq \pi/2$). Note that all

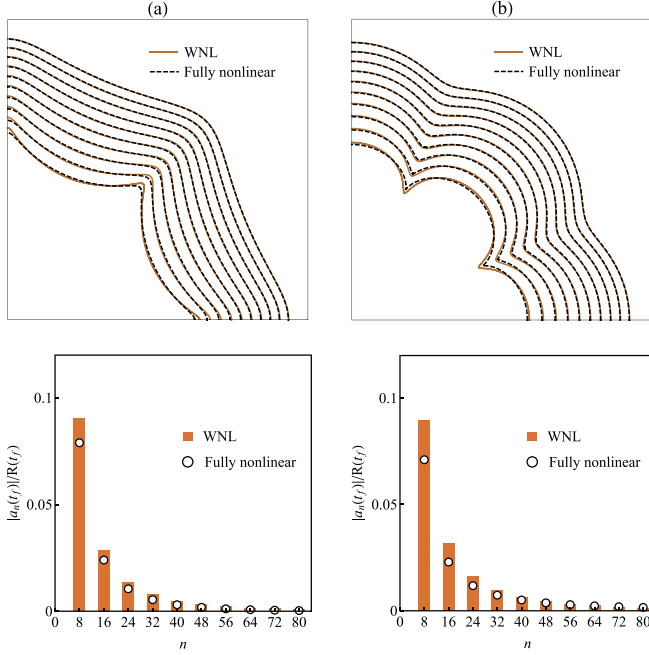


FIG. 9. Weakly and fully nonlinear behaviors for shrinking interfaces in the 2D Stokes flow with suction for (a) $A = 1$, and (b) $A = -1$. Top panels: comparison between weakly nonlinear (WNL, solid curves) and fully nonlinear time evolutions (dashed curves). Bottom panels: corresponding plot of the rescaled cosine mode amplitudes $|a_n(t_f)|/R(t_f)$, taken at the final time $t = t_f$, as a function of the azimuthal mode number n . The small open circles give the values of the rescaled mode amplitudes as extracted directly from the patterns produced by the fully nonlinear calculation. The vertical bars give the corresponding mode amplitudes obtained by our second-order mode-coupling theory. All the other parameters and initial conditions are identical to those used in Fig. 6.

physical parameters and initial conditions used to plot both WNL and fully nonlinear interfaces depicted in Fig. 9 are exactly the same as those used in Fig. 6.

By analyzing the top panels of Fig. 9, we clearly see that the weakly nonlinear theory works well in approaching the fully nonlinear interface shapes, even though only second-order terms are used in our perturbative mode-coupling description. The evolving WNL and fully nonlinear interfaces depart only a bit from each other for later times, and at the location of the emerging near-cusp structures. In such locations, one can verify that the WNL near-cups are a little sharper than their fully nonlinear counterparts. One should not be surprised with these small detected differences between the WNL and fully nonlinear interfaces at later times. After all, in principle, one should not expect that WNL interfacial patterns would precisely reproduce the fully nonlinear morphological features of the near-cusps produced in Refs. [18–22] for all times. Rigorously speaking, our perturbative mode-coupling results are not quantitatively correct at later times, and particularly in the vicinity of near-cusps, since in these locations the interfacial slopes are too large, while perturbatively [Eq. (23)] one should have that $|\mathcal{R}_\theta|/\mathcal{R} \ll 1$. However, as exemplified by the comparisons shown in top panels of Fig. 9, despite its limitations, our second-order mode-coupling theory works

well, reinforcing the reliability of our quadratic truncation. Our perturbative scheme is specially useful in illustrating how the viscosity contrast A influences the shapes of the pattern-forming structures, showing good agreement with previous conforming mapping fully nonlinear calculations for the limiting cases in which $A = \pm 1$. In addition, it is worthwhile to point out once again that the near-cusp phenomena detected in Figs. 6 and 9 for $A = \pm 1$ are inherently nonlinear, and could not be either predicted or captured by a purely linear description of the 2D Stokes problem as previously examined in Refs. [23,24]. These remarks support the usefulness of our present theoretical contribution which extends previous linear analysis of Fourier modes to include key quadratic interactions among the modes.

The bottom panels of Fig. 9 plot the rescaled cosine mode amplitudes $|a_n(t_f)|/R(t_f)$ taken at the final time $t = t_f$, as a function of various azimuthal mode numbers n . The data represented by the small open circles are extracted directly from the patterns produced by the fully nonlinear calculation [Eqs. (35) and (39)]. The Fourier spectrum of the fully nonlinear solutions demonstrates that the mode amplitudes drop quickly as n is increased, in such a way that the fully nonlinear shapes are indeed well described by our weakly nonlinear approach with considers 60 participating modes ($N = 60$). The vertical bars express the approximate values of the mode amplitudes by using the second-order mode-coupling Eqs. (31). Again, one can see that agreement between WNL and fully nonlinear solutions is good. These findings reinforce the reliability of the shape of the WNL Fourier spectra found in Fig. 5. In summary, the results presented in Fig. 9 give quantitative support to the fact that the weakly nonlinear solutions provide a good representation of the fully nonlinear solutions of the 2D Stokes flow problem with suction. We call attention to the fact that we have also compared the time evolution of the WNL patterns illustrated in Fig. 8 for $A = -1$ and several values of the fundamental mode n ($2 \leq n \leq 7$), with their fully nonlinear analogues obtained via Eqs. (35) and (39) (see Fig. 10), and also found good agreement between weakly and fully nonlinear interfacial time evolutions.

We conclude by pointing out that the weakly nonlinear, mode-coupling scheme we use in this work to model the formation of near-cusp patterns in 2D Stokes flows has also been validated over the years by fully nonlinear numerical results for other types of pattern formation problems [44–49]. All these fully nonlinear investigations show that the weakly nonlinear theory is able to correctly capture the onset of pattern formation, providing a reliable way to predict various fundamentally important fully nonlinear, pattern-forming effects.

IV. CONCLUDING REMARKS

Most of the studies of the fingering pattern formation in 2D Stokes flow with suction focus either on the linear stability analysis of the early time dynamics, or on the use of complex variable techniques for the exploration of advanced time stages of the flow. These investigations concentrate their attention basically on two extreme situations: (1) extraction of a bubble of negligible viscosity, for which the viscosity contrast $A = 1$ and (2) contraction of a blob of viscous fluid, for which

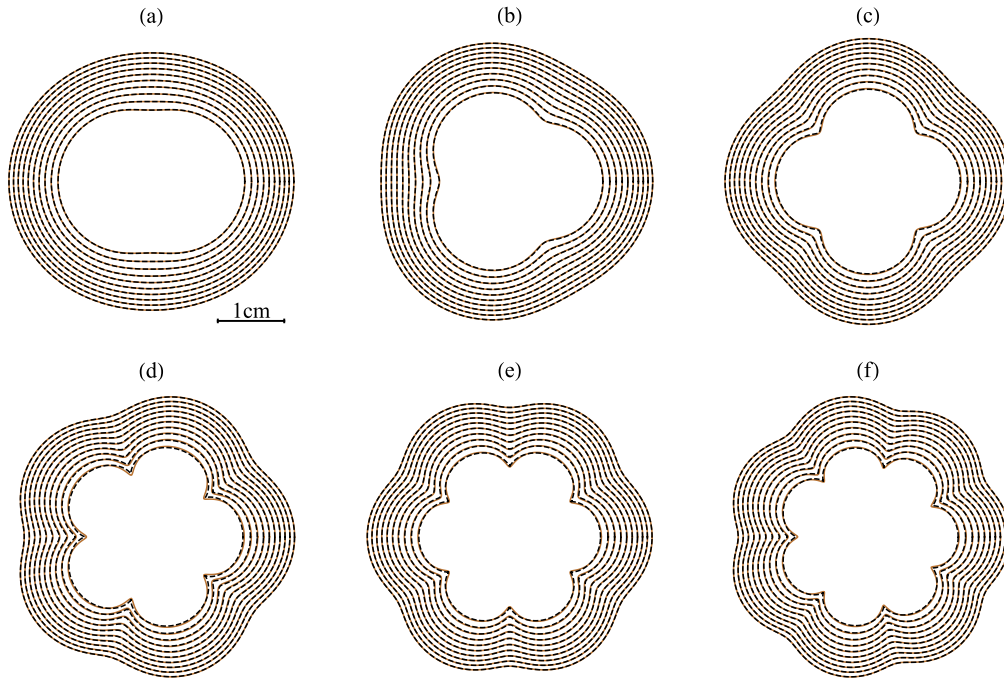


FIG. 10. Comparison between weakly nonlinear (solid curves) and fully nonlinear time evolutions (dashed curves) for shrinking interfaces in the 2D Stokes flow with suction for $A = -1$. As in Fig. 8 the various patterns are obtained by considering that the fundamental mode, and its initial amplitude are taken as (a) $n = 2$, and $a_n(0) = R_0/450$ cm; (b) $n = 3$, and $a_n(0) = R_0/350$ cm; (c) $n = 4$, and $a_n(0) = R_0/280$ cm; (d) $n = 5$, and $a_n(0) = R_0/210$ cm; (e) $n = 6$, and $a_n(0) = R_0/210$ cm; and (f) $n = 7$, and $a_n(0) = R_0/180$ cm. All the other parameters are identical to those utilized in Fig. 8. One can verify that the agreement between weakly and fully nonlinear solutions is good.

$A = -1$. In this work, we examined different aspects of the problem: through the employment of a perturbative, second-order mode-coupling theory, we aim attention at the weakly nonlinear intermediate stages of the flow that bridge purely linear and fully nonlinear regimes. Additionally, instead of examining just the cases for $A = -1$ or $A = 1$, we explored a whole range of permitted values of A (i.e., $-1 \leq A \leq 1$). Our analytical approach provides useful insights into the basic mechanisms of finger-tip sharpening and widening involved in the pattern formation process, and into the role of the viscosity contrast in determining the shape of the emerging fingering structures.

As expressed by the equation of motion for the problem [Eq. (25)], at the linear level, second-order mode-coupling reproduces linear stability results. Accordingly, we derived an expression for the linear growth rate of the 2D Stokes flow problem. This linear dispersion relation reveals some peculiarities if compared with its equivalent expression for the classical Saffman-Taylor problem in radial Hele-Shaw cells. The most salient difference is that, as opposed to what happens in the Saffman-Taylor case, the growth rate for 2D Stokes flow is independent of the viscosity contrast A . Therefore, linearly, A plays no role in the stability of the interface. Different aspects of the linear growth rate have been discussed, a physical mechanism for explaining the Stokes flow instability has been provided, and some other useful information about the linear stability of the system have been extracted. It should be pointed out that the expression of our linear growth rate [Eq. (26)] and our basic linear stability results are in agreement with similar findings previously obtained in

Refs. [23,24,36]. This supports the validity and correctness of our mode-coupling calculation at the linear level.

However, the main contribution of this work refers to our findings at the early nonlinear regime of the dynamics. At the weakly nonlinear level, by utilizing Eq. (25), we have shown that our second-order perturbative interfacial solutions do a decent job in reproducing the highly symmetric, typical fully nonlinear near-cusp morphologies conventionally obtained by analytical and numerical studies based on complex variable methods when $A = 1$ and $A = -1$. This important verification ratifies the validity of our second-order model, reinforcing the fact that the near-cusp weakly nonlinear structures generated in this work offer a good representation of the equivalent fully nonlinear cuspidal patterns previously obtained in the literature [18,19,21,22]. Moreover, we have found that for $-1 < A < 1$, a whole series of unexplored interfacial patterns arise, but at second-order these structures do not display the occurrence of near-cups. Our nonlinear analysis also demonstrates that A has a key role in determining the finger-tip curvature behavior of both inward- and outward-pointing fingers. Furthermore, our second-order findings show that the near-cusps always point from the less to the more viscous fluid, indicating that such interfacial phenomenon is regulated by the viscosity contrast parameter A present in the nonlinear terms of the dynamics [Eq. (27)]. In summary, our perturbative mode-coupling results show that, despite its unimportant value for the linear dynamics, the viscosity contrast is vital in setting the dynamics and shape of interfacial patterns in 2D Stokes flow with suction. It is fortunate, and a bit surprising, that all these relevant aspects about the morphology of the 2D

Stokes flow patterns can be caught and predicted already at the lowest nonlinear level.

Finally, we believe that our analysis could be generalized to the case where one or both fluids are non-Newtonian. As mentioned in the introduction, recent experiments have realized planar viscous flows of shear-thinning fluids, observing the emergence of fingering patterns when a shear-thinning fluid is injected into a less viscous fluid [35,36]. The experimentally found interfaces exhibit fingers with rectangular-shaped tips, which are very different from those obtained here for the suction-driven instability of Newtonian fluids. Note that our perturbative approach is particularly useful in the analysis of instabilities of non-Newtonian flows, since the pressure distribution is not harmonic in those cases, and thus confor-

mal mapping techniques cannot be used to compute the fully nonlinear interfaces.

ACKNOWLEDGMENTS

J.A.M. thanks CNPq (Conselho Nacional de Desenvolvimento Científico e Tecnológico) for financial support under Grant No. 305140/2019-1. G.D.C. also thanks CNPq for financial support of a postdoctoral fellowship under contract No. 150959/2019-2. We gratefully acknowledge important discussions with Carles Blanch-Mercader and Giovanni Vasconcelos. We are indebted to Carles Blanch-Mercader for a critical reading of the manuscript and for providing detailed comments and valuable suggestions.

APPENDIX: EXPRESSIONS FOR $p_{n,1}$, $p_{n,2}$, $u_{n,1}$, $u_{n,2}$

This Appendix presents the expressions for the pressure and velocity Fourier amplitudes which appear in the text:

$$\begin{aligned}
 p_{n,1} = & \eta_1 [n + \text{sgn}(n)] \frac{[n - \text{sgn}(n)]\pi R\sigma + 2\text{sgn}(n)Q(\eta_1 - \eta_2)}{\pi R^3(\eta_1 + \eta_2)} \zeta_n \\
 & - \eta_1 \sum_{n' \neq 0, \pm 1} \left((1 + |n|) \left\{ [(n - n')^2 + n'^2 + |n| - |(n - n')n'| - 2] \frac{\sigma}{R^3(\eta_1 + \eta_2)} \right. \right. \\
 & + 2\eta_2(3 + 3|n| - 2|n - n'| - 2|n'|) \frac{(\eta_1 - \eta_2)Q}{\pi R^4(\eta_1 + \eta_2)^2} \\
 & \left. \left. + 2\eta_1(3 - |n| + 2|n - n'| + 2|n'|) \frac{(\eta_1 - \eta_2)Q}{\pi R^4(\eta_1 + \eta_2)^2} \right\} \right) \zeta_{n-n'} \zeta_{n'}, \quad (\text{A1})
 \end{aligned}$$

$$\begin{aligned}
 p_{n,2} = & -\eta_2 [n - \text{sgn}(n)] \frac{[n + \text{sgn}(n)]\pi R\sigma - 2\text{sgn}(n)Q(\eta_1 - \eta_2)}{\pi R^3(\eta_1 + \eta_2)} \zeta_n \\
 & - \eta_2 \sum_{n' \neq 0, \pm 1} \left((-1 + |n|) \left\{ [(n - n')^2 + n'^2 - |n| - |(n - n')n'| - 2] \frac{\sigma}{R^3(\eta_1 + \eta_2)} \right. \right. \\
 & + 2\eta_1(3 - 3|n| + 2|n - n'| + 2|n'|) \frac{(\eta_1 - \eta_2)Q}{\pi R^4(\eta_1 + \eta_2)^2} \\
 & \left. \left. + 2\eta_2(3 + |n| - 2|n - n'| - 2|n'|) \frac{(\eta_1 - \eta_2)Q}{\pi R^4(\eta_1 + \eta_2)^2} \right\} \right) \zeta_{n-n'} \zeta_{n'}, \quad (\text{A2})
 \end{aligned}$$

$$\begin{aligned}
 b_{n,1} = & -\frac{n\{\text{sgn}(n) + n\}\pi R\sigma + 2\text{sgn}(n)Q(\eta_1 - \eta_2)}{4\pi R^2(\eta_1 + \eta_2)} \zeta_n \\
 & + \sum_{n' \neq 0, \pm 1} \left(n \left\{ [(n - n')^2 + n'^2 + |n| - |(n - n')n'|] \frac{\sigma}{4R^2(\eta_1 + \eta_2)} \right. \right. \\
 & + 2\eta_1(1 - |n| + 2|n - n'| + 2|n'|) \frac{(\eta_1 - \eta_2)Q}{\pi R^3(\eta_1 + \eta_2)^2} \\
 & \left. \left. + 2\eta_2(1 + 3|n| - 2|n - n'| - 2|n'|) \frac{(\eta_1 - \eta_2)Q}{\pi R^3(\eta_1 + \eta_2)^2} \right\} \right) \zeta_{n-n'} \zeta_{n'}, \quad (\text{A3})
 \end{aligned}$$

$$\begin{aligned}
 b_{n,2} = & \frac{n\{-\text{sgn}(n) + n\}\pi R\sigma - 2\text{sgn}(n)Q(\eta_1 - \eta_2)}{4\pi R^2(\eta_1 + \eta_2)} \zeta_n \\
 & + \sum_{n' \neq 0, \pm 1} \left(n \left\{ [(n - n')^2 + n'^2 - |n| - |(n - n')n'|] \frac{\sigma}{4R^2(\eta_1 + \eta_2)} \right. \right. \\
 & + 2\eta_2(1 + |n| - 2|n - n'| - 2|n'|) \frac{(\eta_1 - \eta_2)Q}{\pi R^3(\eta_1 + \eta_2)^2} \\
 & \left. \left. + 2\eta_1(1 - 3|n| + 2|n - n'| + 2|n'|) \frac{(\eta_1 - \eta_2)Q}{\pi R^3(\eta_1 + \eta_2)^2} \right\} \right) \zeta_{n-n'} \zeta_{n'}. \quad (\text{A4})
 \end{aligned}$$

- [1] P. Pelcé, *Dynamics of Curved Fronts* (Academic, Boston, 1988).
- [2] H. Meinhardt, *Models of Biological Pattern Formation* (Academic, New York, 1982).
- [3] M. C. Cross and P. C. Hohenberg, Pattern formation outside of equilibrium, *Rev. Mod. Phys.* **65**, 851 (1993).
- [4] G. Ahlers, D. S. Cannel, M. A. Domingez-Lerma, and R. Heinrichs, Wavenumber selection and Eckhaus instability in Couette-Taylor flow, *Physica D* **23**, 202 (1986).
- [5] P. Manneville, *Dissipative Structures and Weak Turbulence* (Academic, New York, 1990).
- [6] L. Limat, P. Jenffer, B. Dagens, E. Touron, M. Ferm-Cannelligier, and J. E. Wesfreid, Gravitational instabilities of thin liquid layers: Dynamics of pattern selection, *Physica D* **61**, 166 (1992).
- [7] P. G. Saffman and G. I. Taylor, The penetration of a fluid into a porous medium or Hele-Shaw cell containing a more viscous liquid, *Proc. R. Soc. London Ser. A* **245**, 312 (1958).
- [8] For review articles on this subject, see, for example, G. M. Homsy, Viscous fingering in porous media, *Annu. Rev. Fluid Mech.* **19**, 271 (1987); K. V. McCloud and J. V. Maher, Experimental perturbations to Saffman-Taylor flow, *Phys. Rep.* **260**, 139 (1995); J. Casademunt, Viscous fingering as a paradigm of interfacial pattern formation: Recent results and new challenges, *Chaos* **14**, 809 (2004).
- [9] L. Paterson, Radial fingering in a Hele-Shaw cell, *J. Fluid Mech.* **113**, 513 (1981).
- [10] J. D. Chen, Growth of radial viscous fingers in a Hele-Shaw cell, *J. Fluid Mech.* **201**, 223 (1989).
- [11] S. S. S. Cardoso and A. W. Woods, The formation of drops through viscous instability, *J. Fluid Mech.* **289**, 351 (1995).
- [12] J. A. Miranda and M. Widom, Radial fingering in a Hele-Shaw cell: A weakly nonlinear analysis, *Physica D* **120**, 315 (1998).
- [13] O. Praud and H. L. Swinney, Fractal dimension and unscreened angles measured for radial viscous fingering, *Phys. Rev. E* **72**, 011406 (2005).
- [14] S. W. Li, J. S. Lowengrub, J. Fontana, and P. Palfy-Muhoray, Control of Viscous Fingering Patterns in a Radial Hele-Shaw Cell, *Phys. Rev. Lett.* **102**, 174501 (2009).
- [15] I. Bischofberger, R. Ramachandran, and S. R. Nagel, An island of stability in a sea of fingers: Emergent global features of the viscous-flow instability, *Soft Matter* **11**, 7428 (2015).
- [16] H. Thomé, M. Rabaud, V. Hakim, and Y. Couder, The Saffman-Taylor instability: From the linear to the circular geometry, *Phys. Fluids A* **1**, 224 (1989).
- [17] C.-Y. Chen, Y.-S. Huang, and J. A. Miranda, Radial Hele-Shaw flow with suction: Fully nonlinear pattern formation, *Phys. Rev. E* **89**, 053006 (2014).
- [18] S. Tanveer and G. L. Vasconcelos, Time-evolving bubbles in two-dimensional Stokes flow, *J. Fluid Mech.* **301**, 325 (1995).
- [19] S. Tanveer and G. L. Vasconcelos, Bubble Breakup in Two-Dimensional Stokes Flow, *Phys. Rev. Lett.* **73**, 2845 (1994).
- [20] C. Pozrikidis, Numerical studies of cusp formation at fluid interfaces in Stokes flows, *J. Fluid Mech.* **357**, 29 (1998).
- [21] S. D. Howison and S. Richardson, Cusp development in free boundaries, and two-dimensional slow viscous flows, *Eur. J. Appl. Math.* **6**, 441 (1995).
- [22] L. J. Cummings, S. D. Howison, and J. R. King, Two-dimensional Stokes and Hele-Shaw flows with free surfaces, *Eur. J. Appl. Math.* **10**, 635 (1999).
- [23] M. Ben Amar and A. Boudaoud, Suction in Darcy and Stokes interfacial flows: Maximum growth rate versus minimum dissipation, *Eur. Phys. J. Spec. Top.* **166**, 83 (2009).
- [24] M. Ben Amar, J.-M. Allain, N. Puff, and M. I. Angelova, Stokes Instability in Inhomogeneous Membranes: Application to Lipoprotein Suction of Cholesterol-Enriched Domains, *Phys. Rev. Lett.* **99**, 044503 (2007).
- [25] H. A. Stone, A. D. Stroock, and A. Ajdari, Engineering flows in small devices: Microfluidics toward a lab-on-a-chip, *Annu. Rev. Fluid Mech.* **36**, 381 (2004).
- [26] J. P. Rothstein, Slip on superhydrophobic surfaces, *Annu. Rev. Fluid Mech.* **42**, 89 (2010).
- [27] P. Buchak and D. G. Crowdy, Surface-tension-driven Stokes flow: A numerical method based on conformal geometry, *J. Comput. Phys.* **317**, 347 (2016).
- [28] D. Crowdy and E. Luca, Analytical solutions for two-dimensional singly periodic Stokes flow singularity arrays near walls, *J. Eng. Math.* **119**, 199 (2019).
- [29] C. Pozrikidis, Finite deformation of liquid capsules enclosed by elastic membranes in simple shear flow, *J. Fluid Mech.* **297**, 123 (1995).
- [30] M. Higley, M. Siegel, and M. R. Booty, Semi-analytical solutions for two-dimensional elastic capsules in Stokes flow, *Proc. R. Soc. A* **468**, 2915 (2012).
- [31] K. Liu, C. Hamilton, J. Allard, J. Lowengrub, and S. Li, Wrinkling dynamics of fluctuating vesicles in time-dependent viscous flow, *Soft Matter* **12**, 5663 (2016).
- [32] K. Liu, G. R. Marple, J. Allard, S. Li, S. Veerapaneni, and J. Lowengrub, Dynamics of a multicomponent vesicle in shear flow, *Soft Matter* **13**, 3521 (2017).
- [33] K. Pham, E. Turian, K. Liu, S. Li, and J. Lowengrub, Nonlinear studies of tumor morphological stability using a two-fluid flow model, *J. Math. Biol.* **77**, 671 (2018).
- [34] M.-J. Lu, C. Liu, and S. Li, Nonlinear simulation of an elastic tumor-host interface, *Comput. Math. Biophys.* **7**, 25 (2019).
- [35] R. Sayag and M. G. Worster, Instability of radially spreading extensional flows Part I: Experimental analysis, *J. Fluid Mech.* **881**, 722 (2019).
- [36] R. Sayag and M. G. Worster, Instability of radially spreading extensional flows Part II: Theoretical analysis, *J. Fluid Mech.* **881**, 739 (2019).
- [37] R. Sayag, Rifting of Extensional Flows on a Sphere, *Phys. Rev. Lett.* **123**, 214502 (2019).
- [38] G. K. Batchelor, *An Introduction to Fluid Dynamics* (Cambridge University Press, Cambridge, 1967).
- [39] W. E. Langlois and M. O. Deville, *Slow Viscous Flow*, 2nd ed. (Springer, New York, 2014).
- [40] M. Van Dyke, *Perturbation Methods in Fluid Mechanics* (Academic Press, New York, 1964).
- [41] H. Lamb, *Hydrodynamics* (Dover, New York, 1945).
- [42] E. Álvarez-Lacalle, J. Ortín, and J. Casademunt, Nonlinear Saffman-Taylor Instability, *Phys. Rev. Lett.* **92**, 054501 (2004).
- [43] S. Hassani, *Mathematical Physics* (Springer-Verlag, New York, 1998).
- [44] E. Alvarez-Lacalle, E. Pauné, J. Casademunt, and J. Ortín, Systematic weakly nonlinear analysis of radial viscous fingering, *Phys. Rev. E* **68**, 026308 (2003).
- [45] E. Alvarez-Lacalle, J. Casademunt, and J. Ortín, Systematic weakly nonlinear analysis of interfacial instabilities in Hele-Shaw flows, *Phys. Rev. E* **64**, 016302 (2001).

- [46] J. A. Miranda and E. Alvarez-Lacalle, Viscosity contrast effects on fingering formation in rotating Hele-Shaw flows, *Phys. Rev. E* **72**, 026306 (2005).
- [47] P. H. A. Anjos and S. Li, Weakly nonlinear analysis of the Saffman-Taylor problem in a radially spreading fluid annulus, *Phys. Rev. Fluids* **5**, 054002 (2020).
- [48] M. Zhao, P. H. A. Anjos, J. Lowengrub, and S. Li, Pattern formation of the three-layer Saffman-Taylor problem in a radial Hele-Shaw cell, *Phys. Rev. Fluids*, **5**, 124005 (2020).
- [49] R. M. Oliveira and J. A. Miranda, Fully nonlinear simulations of ferrofluid patterns in a radial magnetic field, *Phys. Rev. Fluids* **5**, 124003 (2020).